nature portfolio

https://doi.org/10.1038/s41586-021-03528-w

Supplementary information

Quantum-enhanced nonlinear microscopy

In the format provided by the authors and unedited

Supplementary Information, Quantum-enhanced nonlinear microscopy

Caxtere A. Casacio, Lars S. Madsen, Alex Terrasson, Muhammad Waleed, Kai Barnscheidt, Boris Hage, Michael A. Taylor, and Warwick P. Bowen.

This Supplementary Information provides details about the theory, modelling, and experimental techniques used in the paper "*Quantum-enhanced nonlinear microscopy*".

1 Microscope design

The microscope has an inverted configuration. It is home-built to allow both conventional bright-field imaging and quantum-enhanced stimulated Raman imaging (see Fig. 1**a** in the main text). Near-infrared wavelengths are chosen to minimise laser absorption and photodamage in biological specimens [1, 2]. We employ custom high numerical aperture water immersion microscope objectives to both focus and collect the light. These objectives were made by Leica Microsystems. They were based on Leica HC-PL-APO63x/1.20W objectives, but with custom anti-reflection coating at 1064nm. The choice of high numerical aperture water-immersion objectives ensured tight focussing of the laser fields, and therefore high intensities and spatial resolution. The anti-reflection coatings allowed ultrahigh Stokes transmission of >92%, minimising any degradation in quantum correlations due to microscope losses. Compared to typical high quality objectives with $\sim 65\%$ transmission efficiency, the high transmission of our objectives also increases the number of collected Raman scattered photons by 42%, with a commensurate increase in signal strength. To ensure that the high transmission is maintained in both dry and aqueous media we under-fill the objectives (see Section 6.1).

The objectives have a relatively low $\sim$32% transmission efficiency for pump light. However, the pump intensity is constrained by the photodamage it causes to the sample rather than the laser source (see Fig. 2 of the main text), and is not sent to the detector (see Fig. 1**a** of the main text) so this attenuation of the pump has no consequence for the achievable signal-to-noise.

The objective focus is controlled using a Mad City Labs Nano-F200S focusing module. Samples are positioned with nanometer scale precision using a Mad City Labs Nano-Bio100 stage, which was used to perform raster scanning in imaging experiments. Samples are simultaneously illuminated with incoherent light from a green LED and imaged using a camera (Allied Vision Manta).

2 Laser sources for stimulated Raman excitation

The Stokes laser is provided by a low noise solid-state pulsed laser with 6 ps pulse length, an 80 MHz repetition rate, and a wavelength of $\lambda_{\text{Stokes}} = 1064$ nm (Coherent, Plecter Duo). Part of the laser output is frequency-doubled to 532 nm and used to pump both the home-built squeezer (described below) and a commercial optical parametric oscillator (OPO; APE, Levante Emerald).

The OPO generates a 500 to 700 mW pump laser that is temporally-synchronised and frequency-tuneable over a wavelength range from 750 to 900 nm. This provides the capacity to probe Raman shifts over the range 1713–3935 cm^{-1}.

The pulse duration of the laser source was chosen to be comparable to the decay time of molecular vibrations since this maximises the Raman interaction, with molecular decay times typically in the range of a few picoseconds [3]. The choice of 80 MHz repetition rate is designed to approximately minimise photodamage processes [1]. Lower repetition rates lead to higher peak intensity for a given average intensity, thereby increasing the relative contribution of nonlinear damage processes like ablation, while higher repetition rate increases the relative contribution of linear damage for instance due to heating.

Quantum correlations are generated between photons in the Stokes laser by passing the beam through a home-built squeezed light source, described below.

3 Reaching the shot-noise limit

Many factors can prevent precision optics experiments from operating at the shot-noise floor; most particularly technical laser noise and photodetector electronic noise. Both of these noise sources are especially problematic at low frequencies. To evade low frequency noise, we implement the technique developed in Ref. [3] wherein the pump laser is strongly amplitude modulated. This modulates the stimulated Raman process, shifting the detected signal to sidebands around the modulation frequency, and away from the low frequency laser and electronic noise. In our case we use a resonant electro-optic modulator that provides a high depth of modulation at 20.0083 MHz (approximated as 20 MHz elsewhere in the paper). A custom-built photodetector allows the detection of the sidebands with noise floor dominated by optical shot-noise (or the reduced squeezed noise) and good clearance from both technical laser noise and photodetector electronic noise.

Using this apparatus and approach, we find that the detected Stokes light is shot-noise limited (see Section 8.4). It is then possible to estimate the relative intensity noise $\Delta I/I$ of our stimulated Raman microscope without squeezing. We find $\Delta I/I = (2\hbar c/\eta P \lambda_{\text{Stokes}} \tau)^{1/2} \sim 10^{-8}$, competitive with the best state-of-the-art stimulated Raman microscopes [3, 4], where P =3 mW is the Stokes power reaching the detector, c the speed of light, $\tau = 1$ s is the integration time, and $\eta = 72\%$ the measured quantum efficiency of the photodiode. Using squeezed light further reduces this noise.

4 Stimulated Raman scattering

To detect and characterise the stimulated Raman scattering, the Stokes laser is measured on a resonant feedback photodetector (see Section 8.1) and processed with a spectrum analyser. The average Stokes power reaching the detector is kept constant at 3 mW for all experiments, ensuring both shot-noise limited (or squeezed when the optical parametric amplifier is on) performance and large clearance from the electronic noise of the detector. As discussed above, the stimulated Raman process causes the 20 MHz modulation of the pump field to be imprinted on the Stokes field, with

the size of the imprinted modulation proportional to the strength of Raman scattering. As such, measurement of the 20 MHz modulation of the Stokes field provides a direct measurement of the Raman gain at the frequency shift between the pump and Stokes fields. The Raman spectrum (Fig. 1**b** of the main text) was measured in polystyrene beads by monitoring this 20 MHz signal while adjusting the OPO to sweep the pump laser wavelength between 800 and 816 nm.

5 Sample preparation

The Raman signal is characterized using polystyrene microspheres. Polystyrene has a relatively simple spectrum with strong Raman bands with Raman shifts in the range of 600 to 3100 cm^{-1}, accessible using our pump and Stokes lasers. The uniform composition and size of the beads allows this Raman spectrum, and the photodamage induced by the measurement, to be accurately and reproducibly characterised. It also allows accurate benchmarking of the performance of the microscope.

Polystyrene bead samples were prepared from dry powder of monodisperse spherical polystyrene beads with 3 μm diameter. These were scattered onto a glass coverslip. Vacuum grease was spread around the edge of the coverslip as a sealant, and a second coverslip pressed on top.

For cellular imaging, dehydrated yeast cells (*Saccharomyces cerevisiae*) were sourced from a local supermarket, and hydrated in distilled water mixed with sugar (approximately 0.1% by weight) and NaCl salt (approximately 0.1%) to provide sustenance and prevent osmotic shock. The cells were kept in this media for at least an hour to provide time to recover from dehydration. Cells were then transferred into sample chambers by pipetting 15 μL of the cell solution onto a glass coverslip, adding a sealant of vacuum grease around the outer edge of the coverslip, and then pressing a second coverslip on top. The grease forms a seal around the edge while the cell solution fills the approximately 70 μm gap between the coverslips. The sample was then left to rest for an hour before experiments to provide time for the cells to adhere to the surface, which is necessary for raster imaging. The health of the cell culture was verified separately by adding extra sugar and observing the production of carbon dioxide.

6 Quantifying photodamage

The damage threshold was characterised for samples of 3 μm polystyrene beads. To find the damage threshold, stimulated Raman signals were recorded in beads as the pump power was gradually increased. The Raman signal generally increases with pump power below the damage threshold, but decays after the onset of damage (with an example shown in Fig. 2**a** of the main text). In all cases the damage was confirmed to have occurred by bright-field imaging. This protocol was repeated for 110 particles with the histogram of recorded damage thresholds shown in Fig. 2**b** of the main text.

We verify that photodamage has occurred using bright-field imaging which, for the example measurement in Fig. 2**a** of the main text, shows substantial deformation of the polystyrene bead due

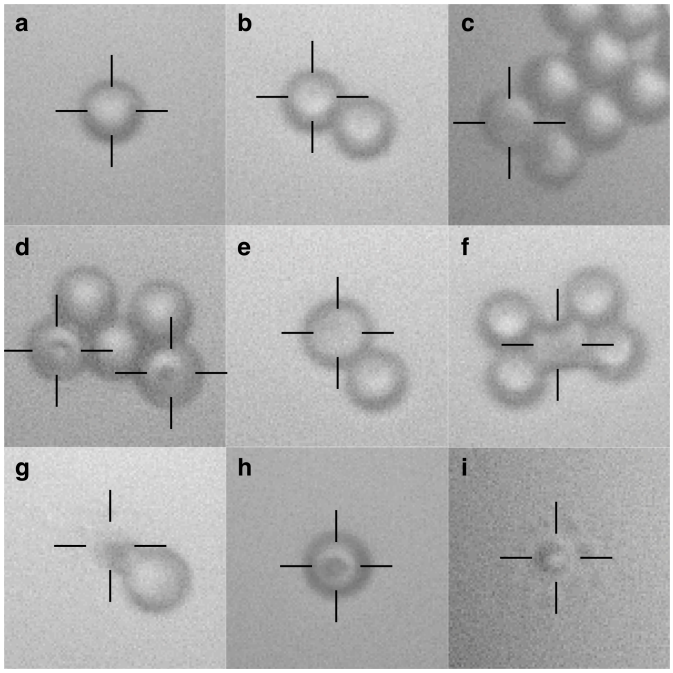

Figure S1: **Bright-field images of typical photodamage.** Examples of the different photodamage modalities that were observed for 3 μm polystyrene beads. **a,** Undamaged bead. **b,** Slight deformation or ablation. **c,** Deformation of target bead and adjacent bead. **d,** Ablation of two beads that were separately exposed. **e,** Deformation. **f,** Significant deformation. **g,** Complete destruction. **h,** Ablation. **i,** Complete disintegration. In each image, the cross-hairs indicate the target bead(s).

to absorptive heating, as well as deformation of an adjacent bead. Measurements on other beads show that other damage modalities also occur, as illustrated by the example bright-field microscope images in Fig. S1, including deformation due to photoabsorptive heating, ablation due to the high peak intensity of the pump laser, and complete destruction/disintegration. The observation of both mean and peak intensity dependent photodamage modalities is an indication that the laser repetition rate and pulse length are well chosen to balance the different classes of photodamage [1].

The distribution of threshold pump intensities at which photodamage occurs shown in Fig. 2**b** of the main text fits well to a Gaussian with mean power at the sample of 54.6 mW and standard deviation of 7.4 mW. The mean power corresponds to a peak pulse intensity of around 150 W/μm^2 consistent with known thresholds for laser ablation [5]. The probability of photodamage is highly sensitive to the optical intensity, as shown by the cumulative probability distribution in Fig. 2**c** of the main text. For instance, when using a pump power of 30 mW none of the polystyrene beads exhibited photodamage, while 26% were damaged at 50 mW.

6.1 Estimating the peak pump intensity at the sample

To estimate the peak pump intensity I_{peak} at the sample from the average pump power at the sample P we assume that the pump pulses have a Gaussian temporal profile with full-width-half-

maximum $t_{\mathrm{FWHM}} = 6$ ps, along with a Gaussian transverse profile with width at the focus w_0. Given the second of assumptions, it is straightforward to show that the peak pump intensity is given by

$$I_{\mathrm{peak}} = \frac{P_{\mathrm{peak}}}{(\pi w_0^2/2)}, \tag{1}$$

where P_{peak} is the peak pump power at the sample. The first assumption allows us to relate the peak power to the average power as

$$P_{\mathrm{peak}} = 2\sqrt{\frac{\ln 2}{\pi}}\frac{\tau}{t_{\mathrm{FWHM}}}P, \tag{2}$$

where here $\tau = 1/(\text{pulse repetition rate in MHz}) = 12.5$ ns is the repetition time of the pump pulse train.

The waist size can be approximated as

$$w_0 = \frac{\lambda_{\mathrm{pump}}}{\pi \mathrm{NA}_{\mathrm{effective}}}, \tag{3}$$

where $\lambda_{\mathrm{pump}} = 1064$ nm is the pump wavelength in vacuum and $\mathrm{NA}_{\mathrm{effective}}$ is the filled numerical aperture of the objective lens. Overfilling the objective was found to introduce background noise due to nonlinear cross-phase modulation effects. All measurements on polystyrene beads were made with an effective numerical aperture of $\mathrm{NA}_{\mathrm{effective}} \sim \mathrm{NA}/2.5 \sim 0.5$, where NA= 1.2 is the numerical aperture of the microscope. The yeast cell images for which no damage was observed were obtained with $\mathrm{NA}_{\mathrm{effective}} \sim 2\mathrm{NA}/3 = 0.8$. The yeast cell images showing photodamage were taken with $\mathrm{NA}_{\mathrm{effective}} \sim \mathrm{NA} = 1.2$, and therefore the intensity increased by a factor of $(3/2)^2 \sim 2$.

7 Production of bright squeezed light

To produce squeezed light we utilise a single pass optical parametric amplifier (OPA) that consists of a second-order nonlinear crystal which is pumped at 532 nm and seeded by the Raman Stokes field at 1064 nm (see Fig. S2). The OPA pump is generated by frequency doubling the 1064 nm light from the Coherent Plecter Duo laser, also used to generate the Stokes field. The nonlinear crystal is a 7 mm long Periodically Polled Potassium Titanyl Phosphate (PPKTP) crystal (Raicol Crystals, s/n:7-112714933). The crystal is temperature stabilised to 32°C to phase match the nonlinear process. The relative phase between the seed and OPA pump is locked using a standard Pound-Drever-Hall type locking system, with a 104.7 kHz modulation applied to the green field, the green light transmitted through the nonlinear crystal detected and demodulated at 104.7 kHz, and the resulting error signal applied back to the phase of the 1064 nm Stokes field. Choosing the sign of the lock correctly allow the squeezing light source to be stably locked to deamplify the Stokes field, leading to amplitude squeezing. The output state is a bright amplitude squeezed state of light which exhibits pair-wise correlations between photons [2].

8 Detecting squeezing and performing quantum-enhanced measurements

To detect the squeezed light, and later to implement quantum-enhanced Raman microscopy, we choose to use a direct detection scheme rather than the usual homodyne detection. Generally homodyne detection is preferred since the interference with the local oscillator both acts to boost the shot-noise of the signal beam above the electronic noise of the detector, and because it provides a straightforward and robust way of determining the shot-noise level, and therefore the level of quantum enhancement[1].

The primary reason to choose direct detection here is that homodyne detection generally requires a local power at least an order of magnitude higher than the signal power. Unlike most experiments with squeezed light, in our experiments the signal power must be relatively high to reach parameter regimes relevant to state-of-the-art Raman microscopy and for which photodamage starts to become apparent. The local oscillator powers required for homodyne detection would then introduce significant challenges in detector design. A second reason to choose direct detection is that it avoids the need to mode-match the signal field to another field after it has passed through the microscope, and therefore relaxes requirements on the beam quality of the transmitted signal field.

[1]By blocking the signal beam, so that the homodyne detects the noise level of the vacuum entering its signal port.

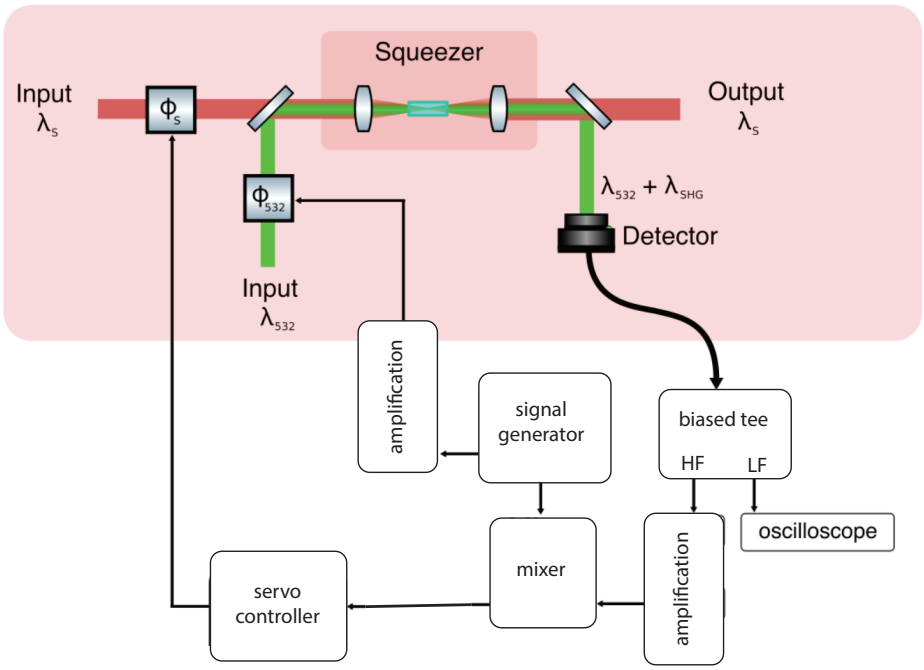

Figure S2: **Schematic of squeezed light source.** ϕ_s: phase shift on 1064 nm Stokes beam. ϕ_{532} phase shift on 532 nm squeezer pump beam. λ_{1064} and λ_{532} wavelengths of Stokes and squeezer pump. LPF: low pass filter. HF: high frequency. LF: low frequency.

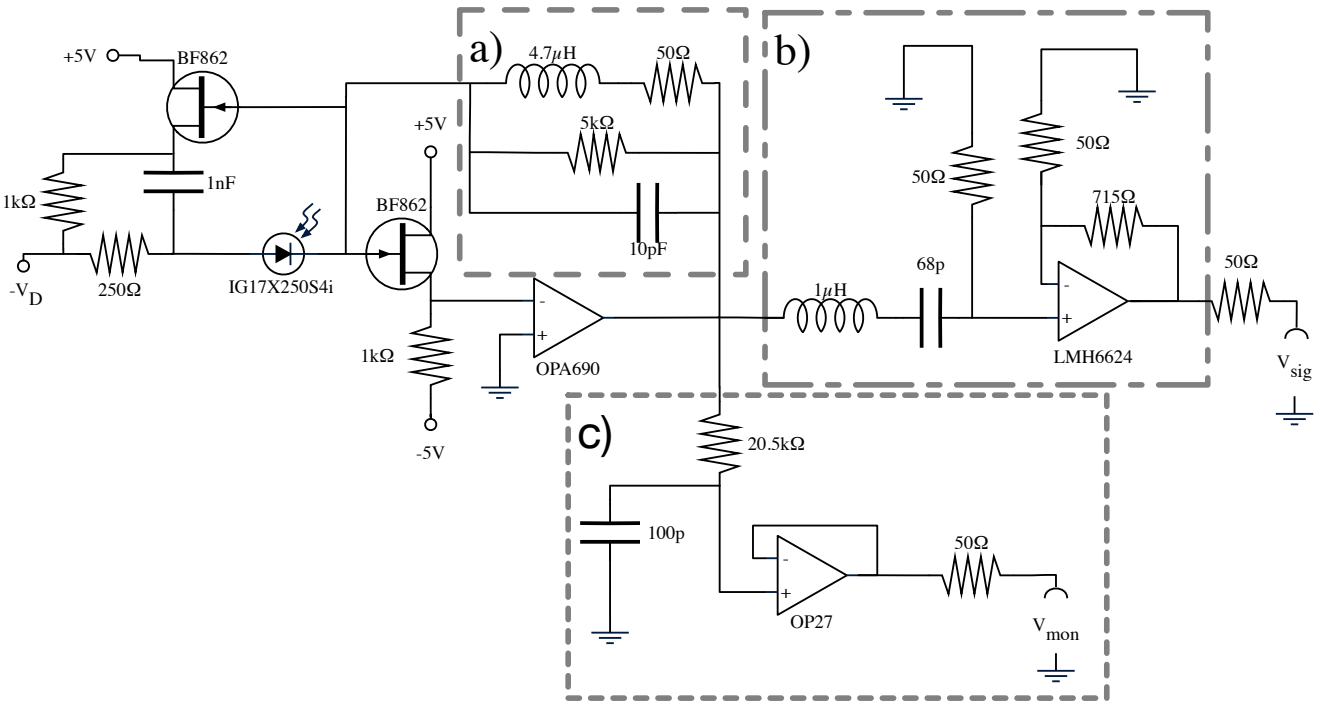

Figure S3: **Detector circuit diagram.** Circuit diagram for the custom-built detector used to detect squeezed light and perform quantum-enhanced Raman microscopy.

8.1 Detector design

To minimise electronic noise and suppress the signal from the laser repetition rate while still providing a high measurement bandwidth, we custom-build a photodetector designed for resonant detection at frequencies around the modulation sideband frequency [6]. Resonant detection is achieved using resonant feedback in a transimpedance amplifier design, as shown in the circuit diagram in Fig. S3. This has several advantages over more commonly used designs, as discussed below.

To avoid saturation due to the large photocurrents, non-resonant detection of pulsed light generally requires a balanced photodiode configuration which subtracts the photocurrents produced by two photodiodes. This cancels both the mean photocurrent and the transient photocurrent at the laser repetition rate, that would otherwise be present. Using resonant feedback eliminates the need for this subtraction by suppressing the response of the photodiode both at DC and above the resonance frequency. This makes it well suited for high power applications that use a single photodiode. Furthermore, compared with typical non-resonant designs based on $\sim 50\ \Omega$ resistive loads, the $\sim 3\ \mathrm{k}\Omega$ resonant feedback impedance converts the photocurrent generated by the detector into a larger voltage. This reduces requirements on the analog filters and buffer amplifiers needed to maintain signal integrity.

Alternative resonant designs use the capacitance of the photodiode paired with a serial inductance to achieve both low noise and high sensitivity on resonance. However, since high intensity ps-pulses create free charges on the diode faster than they can be transported, the capacitance increases as

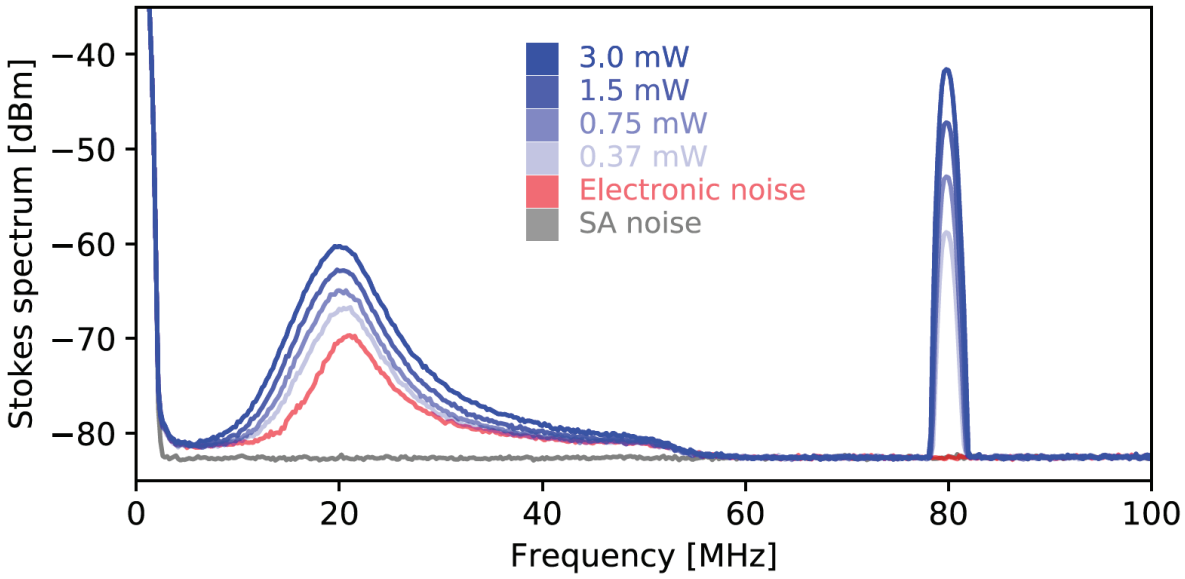

Figure S4: **Raw photocurrent power spectral densities.** Raw power spectral density of photocurrent from custom built resonant detector with no light on the detector (orange), and with increasing Stokes power levels (blue). Grey: spectrum analyser noise floor. RBW: 1 MHz, VBW: 300 Hz.

the voltage across the photodiode drops. The increased capacitance after the pulse leads to a significant shift of the resonance frequency. As this shift depends on the intensity of the pulse, such a design would require adjustments of either the signal frequency or the bias voltage to maintain the resonance condition at different intensity levels.

Since detection efficiency has a direct influence on the achievable quantum enhancement, a InGaAs-PIN photodiode was chosen for the detector. This choice of material generally offers a higher efficiency at 1064 nm than alternative IR-enhanced Si-PIN photodiodes. The higher capacitance per area and lower maximum reverse voltage apply stronger restrictions to the electronic circuit compared to Si photodiodes. However, these photodiode parameters are less critical for resonant feedback detector than other resonant designs since the resonance frequency is determined predominantly by the feedback. State-of-the-art stimulated Raman microscopes require photodetectors that have high power handling to maximise the useable Stokes laser power and therefore signal-to-noise, high bandwidth to maximise the achievable imaging frame rate, and low electronic noise [4]. As a compromise between these requirements, we choose a photodiode of 250 μm diameter, with larger diameter allowing better power handling at the cost of slower response and higher electronic noise.

8.2 Detector performance

The raw power spectra observed for different Stokes power levels in the absence of squeezing are compared to the electronic noise floor of the detector in Fig. S4. When detecting 3 mW of Stokes light we find that laser noise dominates electronic noise over a wide frequency band, from 9 to

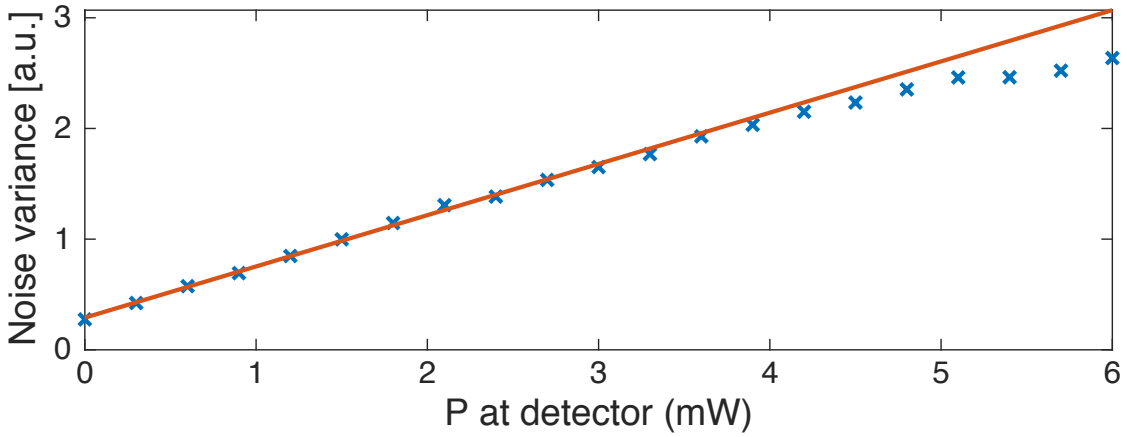

Figure S5: **Stokes laser is shot-noise limited.** Power scaling of Stokes laser noise variance without squeezing, detected with our custom-built resonant feedback stimulated Raman photodetector. The variance is measured at the stimulated Raman modulation sideband frequency of 20.0083 MHz using a spectrum analyser with 1 kHz resolution bandwidth, matching the resolution bandwidth used to take data in the main text. Red line: linear fit to the expected scaling for shot-noise, excluding measurement points at high powers where the photodetector saturates.

40 MHz. The peaks in the electronic noise and Stokes noise variances at around 21 MHz are due to the resonant design of the photodetector. The sharp peak in the Stokes variance at 80 MHz corresponds to the repetition rate of the laser.

8.3 Characterisation of quantum-enhancement

Throughout the paper, the noise reduction due to quantum correlations was assessed by analysing the noise variance of the photocurrent from the resonant feedback photodetector using a spectrum analyser. The noise was calibrated against shot-noise using the Stokes laser with squeezer switched off as a reference, since this was known to be shot-noise limited (see below). To ensure a fair comparison, the same Stokes power of 3 mW is used at the photodetector with both squeezer on and off. All reported noise floor reductions are raw: that is, the electronic noise of the photodetector and spectrum analyser is not removed. As such, the measurements represent the actual useful improvement in noise floor that is achieved, rather than the ideal improvement that would be possible if there was no electronic noise.

The most direct method to determine the quantum enhancement of the stimulated Raman microscope would be to compare identical measurements with and without squeezing of the Stokes field. However, the Raman scattering signal depends on the spatiotemporal modeshape of the Stokes field, since this affects the Stokes intensity at the sample, the spatiotemporal overlap of the Stokes field with the Raman pump, and how well matched the Stokes pulse duration is to the coherence time of the molecular vibration. Consequently, if the comparison involved the Raman signal (for instance, a direct comparison of signal-to-noise ratios), it would be crucial to ensure that the spatiotemporal modeshape of the Stokes field remain unchanged when the squeezing is switched on – any modification of the modeshape would alter the Raman signal size in a purely classical

way, which should not be misinterpreted as a quantum enhancement (or dehancement) due to the presence of correlated photons. Maintaining identical spatiotemporal profiles with and without squeezing proved not to be possible in practise due to the non-perfect spatiotemporal overlap between the 532 nm OPA pump laser and the Stokes field within the squeezing crystal. The effect of this non-perfect overlap is explored in some detail in Section 9.2 below. The important concept, here, is that only the component of the Stokes field that is overlapped with the OPA pump is deamplified, with the non-overlapped component left to transmit through the crystal unaffected. When the squeezer is switched on, the deamplification reduces the overlapped Stokes intensity by more than 50% (see Fig. S9**b**) but leaves the non-overlapped component unchanged. This changes the spatiotemporal modeshape of the Stokes field.

We found experimentally that the change in Stokes field spatiotemporal modeshape due to deamplification caused some modifications to the Raman signal strength. Generally, the signal strength was degraded by these changes. This is most likely due to a reduction in peak Stokes intensity – the Stokes field experiences maximum deamplification at the spatiotemporal peak of the OPA pump pulse and less amplification in the wings of the pulse, this broaden it in both space and time. We note that, even with the degradation in signal strength due to deamplification, due to the quantum-enhancement of the noise floor it was possible to achieve higher signal-to-noise using squeezing than without it. For instance, Fig. S6 shows an example measurement of the Raman signal and noise floor for the CH aromatic stretch band (Raman shift of 3055 cm^{-1}) in polystyrene, with and without squeezing. We see that, while the Stokes spatiotemporal modeshape modification due to deamplification reduces the signal strength by 10%, the improved noise floor due to squeezing still allows a 4% improvement in the signal-to-noise ratio. Moreover, the degradation in signal strength is not fundamental – it could be compensated for using different Stokes focussing or applying pulse shaping techniques without compromising the quantum correlations that provide a quantum-enhanced noise floor.

To achieve a comparison of the signal-to-noise enhancement that is insensitive to classical variations in signal strength, accessing the underlying quantum enhancement; rather than directly measuring the Raman signal strength both with and without squeezing, we only measure the Raman signal strength S with the squeezer on. We assume that, for identical Stokes spatiotemporal modeshape, the signal when using shot-noise limited light will have the same magnitude. This is an appropriate assumption, since the scattering cross-section, and therefore number of pump photons Raman scattered into the Stokes field, is independent of quantum correlations between photons in the Stokes field. We note that this assumption and approach has been used to characterise the quantum enhancement in other work for similar reasons [7]. The quantum enhanced signal-to-noise ratio in Fig. 3**c** of the main text is then directly calculated as $\mathrm{SNR}^{\mathrm{quantum}} = \mathrm{S}/\mathrm{N}^{\mathrm{quantum}}$, where $\mathrm{N}^{\mathrm{quantum}}$ is the noise floor of the quantum-enhanced measurement; with the shot-noise limited signal-to-noise calculated as $\mathrm{SNR}^{\mathrm{shot-noise}} = \mathrm{S}/\mathrm{N}^{\mathrm{shot-noise}} = \mathrm{SNR}^{\mathrm{quantum}} \times \mathrm{N}^{\mathrm{quantum}}/\mathrm{N}^{\mathrm{shot-noise}}$, where $\mathrm{N}^{\mathrm{quantum}}$ is the noise floor of the shot-noise limited measurement. Similarly, for the imaging in Fig. 4 of the main text, the image is normalised to the shot-noise floor by dividing the Raman signal observed with quantum-enhancement by the shot-noise floor determined by both switching the squeezer off and blocking the Raman pump field. The method we employ provides a comparison of the signal-to-noise ratios that would be achieved with and without squeezing if identical spatiotemporal modeshapes were used. As well as providing a fair "apple-to-apple" comparison, by separating the quantum and classical effects it accesses the underlying quantum enhancement of the noise floor independent of the specifics of the particular molecular vibration probed or the optical focussing

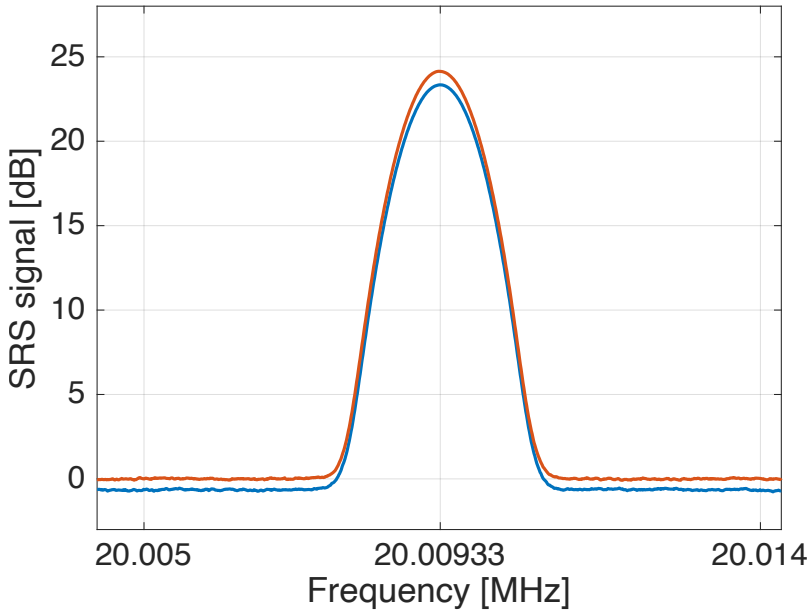

Figure S6: **Stimulated Raman signal-to-noise with and without squeezing.** Example power spectral density of the detected photocurrent showing the stimulated Raman signal and noise floor for both quantum-enhanced (blue) and shot-noise-limited (red) measurements. The quantum-enhanced measurement has a signal-to-noise-ratio of 260, while the signal-to-noise of the shot-noise-limited measurement is 250. The measurements were performed sequentially on the CH aromatic stretch band (Raman shift of 3055 cm^{-1}) in polystyrene. 30 mW of pump power and 3 mW of Stokes power were used. Quantum correlations suppressed the noise floor of the quantum-enhanced measurement by 14% (-0.64 dB). When using squeezed light, classical spatiotemporal modeshape differences degrade the Raman signal strength by 10%. Even taking this classical degradation into account, the signal-to-noise is enhanced by 4% when using squeezed light. RBW: 1 kHz. VBW: 10 Hz.

into the microscope.

8.4 Verification that the Stokes laser is shot-noise limited

To verify that the Stokes laser is shot-noise limited when the squeezer switched off, as is critical when using it for noise calibration, we measure the variance of its noise as a function of power. This is shown in the power spectra in Fig. S4. Over the full range of frequencies where the light noise dominates the electronic noise, the light noise was found to scale linearly with Stokes power for powers beneath detector saturation. This linear scaling is consistent with expectations for a shot-noise limited laser. If the laser were instead limited by technical noise, such as laser relaxation oscillation or spontaneous emission noise, quadratic scaling would be expected.

Most important for the experiments reported here, is that prior to squeezing the Stokes light is shot-noise limited around the stimulated Raman modulation frequency. Measurements at that frequency are shown as a function of power in Fig. S5. Linear scaling is observed for optical powers below 4 mW, with detector saturation occurring at higher powers. As can be seen, that data is inconsistent with the quadratic scaling expected for technical noise. As such it may be concluded that with the squeezer switched off the Stokes laser is shot-noise limited at the 3 mW power levels used in our experiments.

9 Measurement and validation of squeezing

9.1 Observed squeezing spectrum

Fig. S7 shows a typical observed raw power spectrum of the squeezed light generation in our OPA, compared to both the electronic noise floor of the detector and the shot-noise of the Stokes laser observed with the same 3 mW of power incident on the detector. It can be seen that the noise on the squeezed field is suppressed compared to the shot-noise limit over a wide frequency range. Fig, 3**a,** in the main text normalises the squeezing to the shot-noise level to show the quantum noise reduction more clearly as a function of frequency. In this figure, and for all reported quantum-enhancement values, electronic noise is not corrected for; that is, the quantum enhancement reported is the real enhancement of the measurement, not the enhancement that would be achieved if the detector was replaced with an ideal detector with no electronic noise. As can be seen in that figure, suppression of the noise beneath the shot-noise level is achieved for frequencies between 5 MHz and 52 MHz, though it is degraded at the extremes due to the electronic noise of the detector. As such, the quantum enhancement we observe could be applied in scenarios with sub-microsecond pixel dwell times, allowing video rate stimulated Raman imaging.

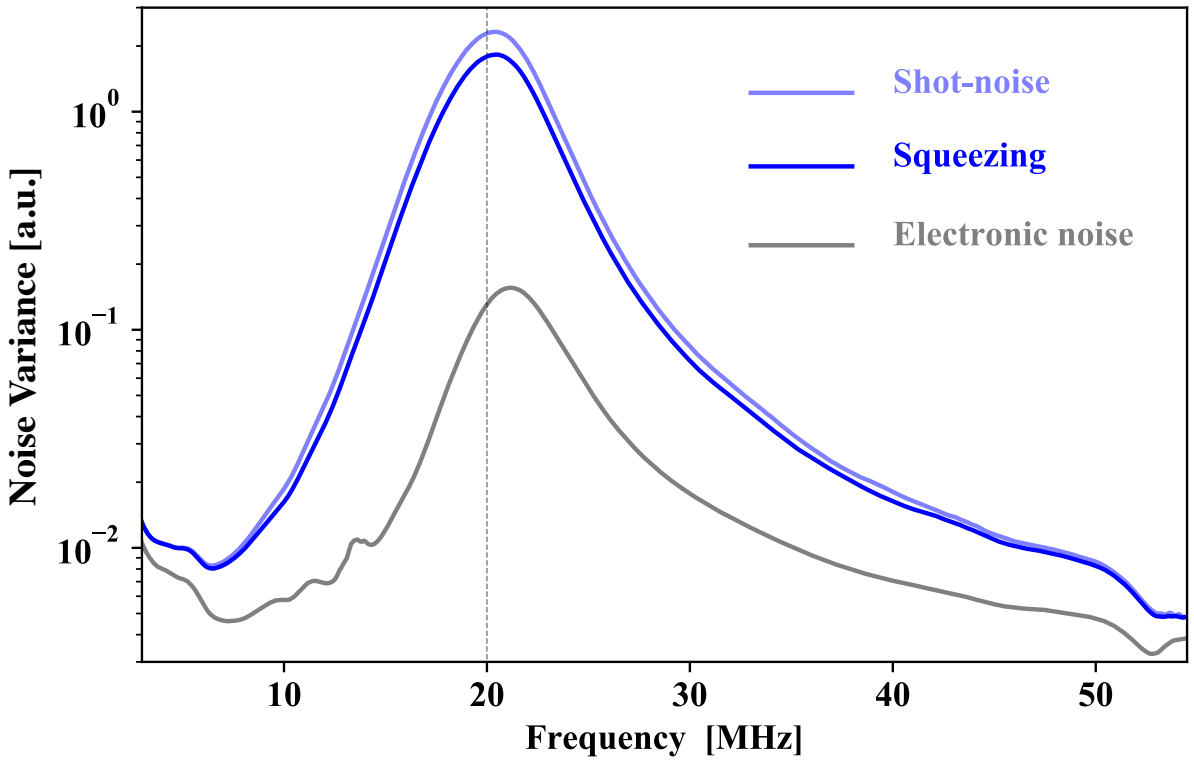

Figure S7: **Raw photocurrent power spectral densities using squeezed and shot-noise limited light.** Raw power spectral density of photocurrent from custom built resonant detector with no light on the detector (grey), 3 mW of shot-noise limited light on the detector (light blue), and 3 mW of amplitude squeezed light on the detector (dark blue). RBW: 1 MHz. VBW: 10 Hz. Averaged thirty five times.

9.2 Modelling the squeezing process

As described above and in the main text, to produce squeezed light we utilise a single pass optical parametric amplifier. The simplicity of a single-pass configuration makes it technically desirable from alignment, construction and control perspectives. It is possible here, since the use of picosecond pulses increases the peak intensity of the light, and therefore the nonlinear interaction, making resonant enhancement in a cavity redundant. However, the lack of an optical cavity also introduces the possibility of multi-spatial mode effects which could potentially deleteriously effect the level of squeezing generated. To investigate this, and confirm that the squeezing generation is well understood, we develop consider a simple model of the squeezing process, taking account of non-perfect spatial overlap between the OPA pump field and the Stokes field.

The concept of the model is shown in Fig. S8. Fig. S8a shows a rough schematic of the squeezer with OPA pump and Stokes partially misaligned. Only the spatially overlapped component of the Stoke laser will experience amplification due to the pump. The non-overlapped component will pass through the nonlinear crystal unaffected. Fig. S8b shows a basic model of this, with a fraction η_{overlap} of the Stokes field perfectly overlapped with the OPA pump, and a fraction $1 - \eta_{\text{overlap}}$ bypassing the pump entirely. Both component of the field then propagate towards the photodetector, and reach it with the same transmission efficiency η_{det} (including the inefficiency of the photodetector itself). They are then detected together on the photodetector.

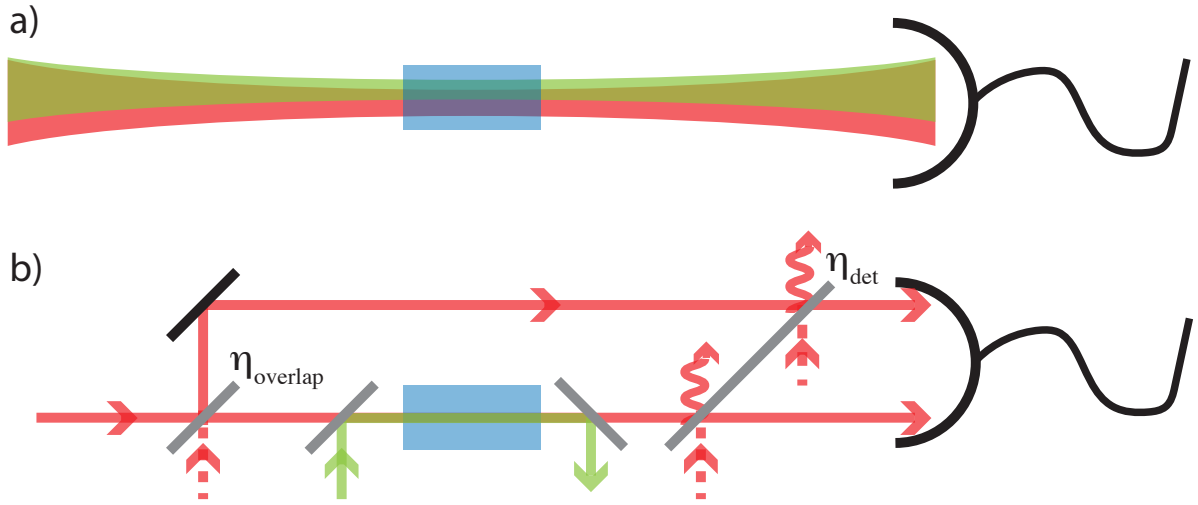

Figure S8: **Model of squeezing process. a,** Schematic showing that the pump (shaded in green) and seed (shaded in red) fields incident on the nonlinear crystal that performs optical parametric amplification are not perfectly overlapped. The red field is detected directly on a photodiode. **b,** The non-perfect overlap can be modelled by treating a fraction of the seed light (given by η_{overlap}) as perfectly overlapped, and a fraction as bypassing the nonlinear crystal entirely. Since the direct detection detects both components of the seed field, and these components are orthogonal, the photocurrents they create can be added together to determine the total detected photocurrent. Detection inefficiency is modelled by including beam splitters into each of the two components, both with transmission efficiency given by η_{det}.

The amplitude $\hat{X}_1$ and phase $\hat{Y}_1$ quadratures of the component of the detected light that does not experience squeezing are given by

$$\hat{X}_1 = \sqrt{\eta_{\rm det}}\left(\sqrt{1-\eta_{\rm overlap}}\hat{X}_{\rm in} - \sqrt{\eta_{\rm overlap}}\hat{X}_{v1}\right) + \sqrt{1-\eta_{\rm det}}\hat{X}_{v2} \quad (4)$$

$$\hat{Y}_1 = \sqrt{\eta_{\rm det}}\left(\sqrt{1-\eta_{\rm overlap}}\hat{Y}_{\rm in} - \sqrt{\eta_{\rm overlap}}\hat{Y}_{v1}\right) + \sqrt{1-\eta_{\rm det}}\hat{Y}_{v2}, \quad (5)$$

where $\hat{X}_{\rm in}$ and $\hat{Y}_{\rm in}$ are the amplitude and phase quadratures of the input Stokes light, and the subscripts $v1$ and $v2$ label the vacuum noise entering due to poor overlap and transmission inefficiency, respectively.

Similarly, the amplitude $\hat{X}_2$ and phase $\hat{Y}_2$ quadratures of the component of the detected light that is perfectly overlapped to experience squeezing are given by

$$\hat{X}_2 = \sqrt{G\eta_{\rm det}}\left(\sqrt{\eta_{\rm overlap}}\hat{X}_{\rm in} + \sqrt{1-\eta_{\rm overlap}}\hat{X}_{v1}\right) + \sqrt{1-\eta_{\rm det}}\hat{X}_{v3} \quad (6)$$

$$\hat{Y}_2 = \sqrt{\frac{\eta_{\rm det}}{G}}\left(\sqrt{\eta_{\rm overlap}}\hat{Y}_{\rm in} + \sqrt{1-\eta_{\rm overlap}}\hat{Y}_{v1}\right) + \sqrt{1-\eta_{\rm det}}\hat{Y}_{v3}, \quad (7)$$

where the subscript $v3$ labels the vacuum noise entering due to transmission inefficiency for this field, and G is the level of squeezing of the variance of the perfectly overlapped squeezed light, prior to detection inefficiencies. Here, $G < 1$ for amplitude squeezing.

Since the perfectly overlapped and non-overlapped fields are spatially orthogonal, when they are detected together on the photodiode they do not interfere, so that the resulting photocurrent is simply the sum of the photocurrents that would be measured if each was detected independently:

$$i = a_1^\dagger a_1 + a_2^\dagger a_2 \quad (8)$$

$$= \alpha_1^2 + \alpha_2^2 + \alpha_1\delta\hat{X}_1 + \alpha_2\delta\hat{X}_2, \quad (9)$$

where the a's are annihilation operators for the fields, with $\hat{X} = a + a^\dagger$ and $\hat{Y} = i(a^\dagger - a)$, the coherent amplitude is defined as $\alpha = \langle a\rangle$ and is defined here to be real without loss of generality, and the noise operators are defined as $\delta\hat{X} = \hat{X} - \langle\hat{X}\rangle$ so that $\langle\delta\hat{X}\rangle = 0$. Here, to get to Eq. (9) we have used the usual linearisation approximation, assuming that $\{\alpha_1, \alpha_2\} \gg 1$ so that noise operator product terms can be neglected.

The squeezer acts to both deamplify the coherent amplitude of the Stokes field and decrease its noise variance. The deamplification is given by

$$D = \frac{\langle i\rangle}{\langle i\rangle_{G=1}} = \frac{\alpha_1^2 + \alpha_2^2}{\alpha_1^2 + \alpha_{2,G=1}^2}. \quad (10)$$

The fractional reduction in noise variance beneath the shot-noise level is

$$V = \frac{\langle i^2\rangle - \langle i\rangle^2}{(\langle i^2\rangle - \langle i\rangle^2)_{G=1}} = \frac{\alpha_1^2 + \alpha_2^2 V_2}{\alpha_1^2 + \alpha_2^2} \quad (11)$$

where we have used the fact that the noise operators of the perfectly-overlapped and non-overlapped fields are uncorrelated, have defined the shot-noise limited variance of the non-overlapped field $V_1 = \langle\delta\hat{X}_2^2\rangle$ to equal one, and $V_2 = \langle\delta\hat{X}_2^2\rangle$ is the variance of the detected perfectly-overlapped

squeezed component in the absence of the non-overlapped field. We have also used the fact that when the squeezer is switched off ($G = 1$) the overlapped field is shot-noise limited so that $V_2 = 1$.

To determine the effect of mode mismatch and detection inefficiency on the observed amplification and squeezing, we therefore need to determine α_1, α_2 and V_2. From Eqs. (4) and (6), the detected coherent amplitudes of the non-overlapped and perfectly overlapped fields when detected can be shown to be

$$\alpha_1 = \sqrt{\eta_{\rm det}(1-\eta_{\rm overlap})}\alpha_{\rm in} \tag{12}$$

$$\alpha_2 = \sqrt{G\eta_{\rm det}\eta_{\rm overlap}}\alpha_{\rm in}, \tag{13}$$

and the squeezing of the perfectly overlapped field to be

$$V_2 = G\eta_{\rm det} + 1 - \eta_{\rm det}, \tag{14}$$

where we have appropriately taken the input field and vacuum noise inputs to be shot-noise limited ($\langle\delta\hat{X}^2_{\rm in}\rangle = \langle\delta\hat{X}^2_{v1}\rangle = \langle\delta\hat{X}^2_{v3}\rangle = 1$) and uncorrelated with each other.

Substituting these expressions into Eqs. (10) and (11) we find

$$D = 1 - \eta_{\rm overlap} + G\eta_{\rm overlap}, \tag{15}$$

and

$$V = \eta_{\rm det}\left(\frac{1-\eta_{\rm overlap}+\eta_{\rm overlap}G^2}{1-\eta_{\rm overlap}+\eta_{\rm overlap}G}\right) + 1 - \eta_{\rm det}. \tag{16}$$

As expected, we see that the deamplification is independent of detection efficiency - the detection inefficiency affects the coherent amplitude in exactly the same way independent of whether the light is squeezed or not. As $G \to 0$ the deamplification asymptotes to $1 - \eta_{\rm overlap}$. This makes sense, since in that limit the spatially overlapped fraction of the light is perfectly deamplified, while the non-overlapped component remains unaffected.

The predicted noise variance V exhibits behaviour unexpected from a normal single-mode squeezer. Instead of the variance decreasing monotonically as $G \to 0$ from above, it decreases below the shot-noise limit and then rises again to exactly the shot-noise limit ($V = 1$) at $G = 0$. This can be understood since, as discussed above, in this limit the coherent amplitude of the squeezed component goes to zero. Since the magnitude of the detected photocurrent scales with the coherent amplitude, the squeezed-light signal in the photocurrent is fully suppressed, only leaving the signal from the shot-noise limited field that has no overlap. We note that this deleterious effect could be avoided in future quantum-enhanced nonlinear microscopes by using a homodyne configuration, and carefully mode matching the local oscillator field to only the squeezed component of the Stokes field. Improvements in the observed squeezing could be obtained not only by controlling the transverse spatial modeshape of the local oscillator, but also by engineering its temporal modeshape. The pulsing of the parametric amplifier pump field leads to a time dependent parametric gain, with the highest deamplification occurring at the peak of the pulse. As a consequence, the squeezing of the Stokes field can be expected to be strongest near the peak of the pulse. An appropriately temporally tailored local oscillator could extract out this highly squeezed component of the Stokes field, lowering the measurement noise floor.

It is straightforward to calculate the gain at which the squeezing is maximised as well as the maximum squeezing. Doing this, we find

$$G_{\min \mathrm{V}} = \frac{\sqrt{1-\eta_{\mathrm{overlap}}}}{\eta_{\mathrm{overlap}}}\left(1-\sqrt{1-\eta_{\mathrm{overlap}}}\right) \tag{17}$$

$$V_{\min} = 2G_{\min \mathrm{V}} = \frac{2\sqrt{1-\eta_{\mathrm{overlap}}}}{\eta_{\mathrm{overlap}}}\left(1-\sqrt{1-\eta_{\mathrm{overlap}}}\right). \tag{18}$$

Assuming no pump depletion, which is reasonable in our case, the seed light (the input Stokes field) is exponentially amplified as it propagates through the OPA crystal to produce the gain G on the final output amplitude quadrature (and $1/G$ on the phase quadrature). The gain can then be expressed as $G = e^{-\kappa L}$ where κ is the gain per unit length and L is the length of the crystal. Recognising that the nonlinear interaction is proportional to the amplitude of the OPA pump field, so that $\kappa \propto \sqrt{P}$ where P is the OPA pump power, this can be re-expressed as $G = e^{-g\sqrt{P}}$, where g is a gain coefficient that depends on the length, phase matching and nonlinear coefficient of the crystal, as well as the optical focussing within the crystal. With this relationship it is possible to compare the predictions of the model to experiment.

9.3 Comparison of model and experiment

To compare model and experiment we measure both the deamplification and squeezing as the pump power is varied from 0 to 70 mW. The results are shown in Fig. S9. We fit the deamplification to Eq. (15) extracting the overlap efficiency $\eta_o = 0.85 \pm 0.02$ and gain coefficient $g = 8.8 \pm 0.4\ \mathrm{W}^{-1/2}$. Fixing these parameters and fitting the squeezed variance to Eq. (16) we determine the detection efficiency in this case (without passing through the microscope) to be $\eta_d = 0.65 \pm 0.01$, consistent with expectations given the measured 72% efficiency of the detector and inefficiencies in transmission from the nonlinear crystal to the detector. As can be seen from Fig. S9, the data agrees well with the theory[2], validating this simple model. The agreement also provides further validations that, prior to the squeezing process, the Stokes field is shot-noise limited and that our method of determining the quantum enhancement is accurate.

As can be seen in Fig. S9 the variance of the detecter squeezing is optimised and relatively insensitive to OPA pump power in the power range between 35 and 65 mW. We therefore operate our experiments in this regime.

10 Total detection efficiency of squeezed light

Optical inefficiencies reduce quantum correlations between photons and therefore degrade the level of quantum enhancement that is possible using squeezed light. The path between the nonlinear crystal generating squeezing and eventual photodetection, included a range of optical elements

[2]We note that the variance data disagrees with more basic theory that does not account for the effect of deamplification of the coherent amplitude of the overlapped field on the detected variance.

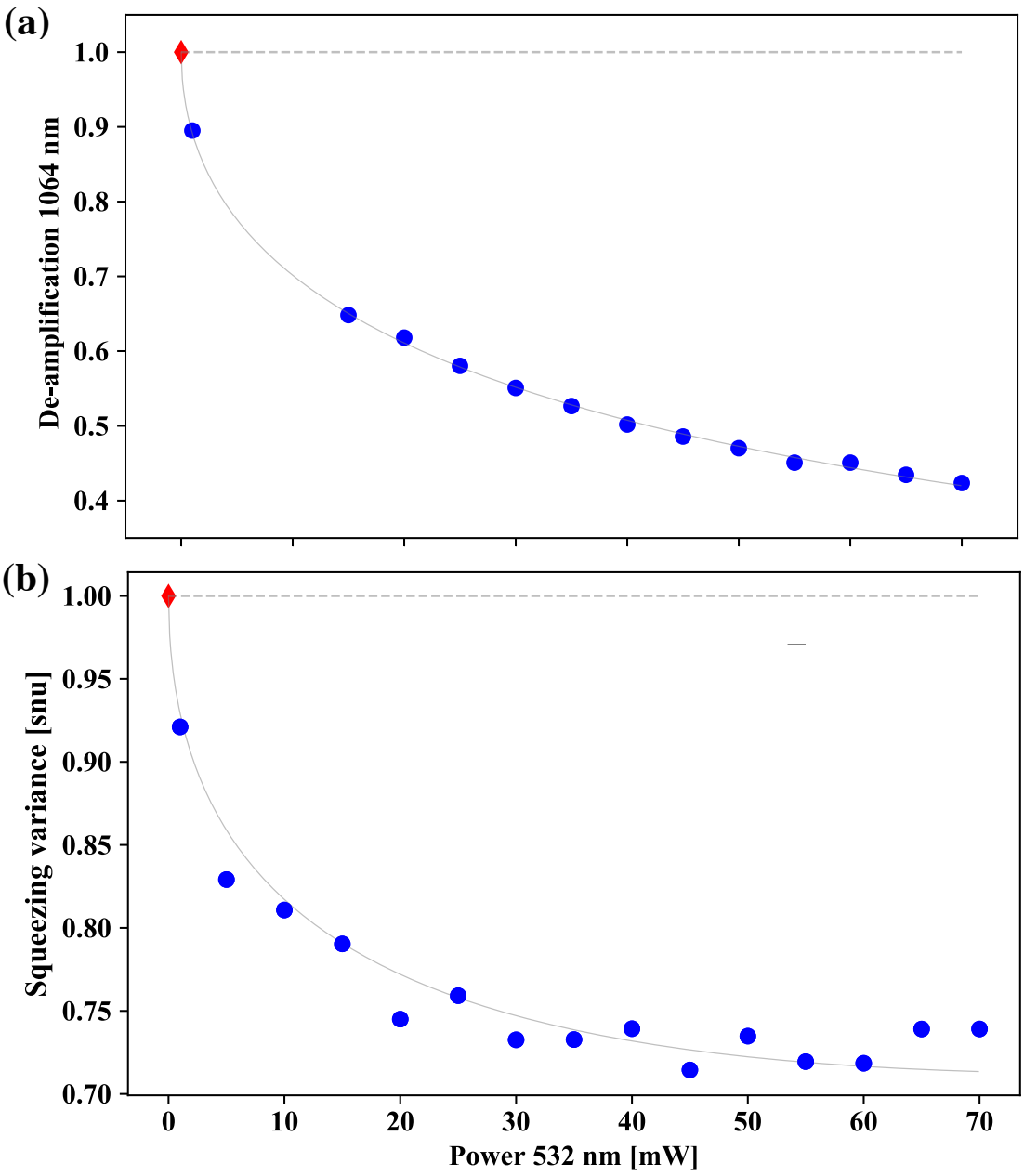

Figure S9: **Validating the model and characterizing the performance of the squeezer.** (a) Measured reduction in the intensity of the seed field after the OPA as a function of OPA pump power. Line: least squares fit to data with the overlap efficiency η_{overlap} and squeezer gain g as fitting parameters. The fit yielded values of $\eta_{\text{overlap}} = 0.85 \pm 0.02$ and $g = 8.8 \pm 0.4$ W$^{-1/2}$. (b) Observed squeezed variance at 20 MHz as a function of OPA pump power. Line: least squares fit to data with only the detection efficiency η_{det} as a free parameter, $\eta_{\text{overlap}} = 0.85$, and $g = 8.8$ W$^{-1/2}$. The fit yielded $\eta_{\text{det}} = 0.65 \pm 0.01$. snu: shot-noise units.

which introduce loss, as shown schematically in Fig. 1**a** of the main text. The microscope itself was a significant source of loss, in the objectives, in dichroic mirrors, and due to reflections from the microscope coverslips. The total efficiency of transmission through the microscope was measured to be $\eta_{\text{microscope}} = 0.75$. The mirrors, lenses and dichroic mirrors between the nonlinear crystal and microscope and between the microscope and photodetector were measured to have transmission of $\eta_{\text{propagation}} = 0.82$. The photodetector efficiency was determined by measuring photocurrent i produced by $P_{\text{Stokes}} = 3$ mW of Stokes light and comparing the flux of electrons this corresponds to to the flux of photons arriving at the detector. The measured photocurrent of $i = 1.86$ mA resulted in a detector quantum efficiency of

$$\eta_{\text{detector}} = \frac{\hbar\omega}{P_{\text{Stokes}}} \times \frac{i}{e} = 0.72, \tag{19}$$

where e is the charge on an electron, $\hbar$ is the reduced Plancks constant, and $\omega = 2\pi c/\lambda$ is the angular optical frequency, with c the speed of light and $\lambda = 1064$ nm the Stokes wavelength. Combined, this gives a total efficiency of transmission of the squeezed light from the nonlinear crystal to the measured photocurrent of

$$\eta = \eta_{\text{microscope}}\eta_{\text{propagation}}\eta_{\text{detector}} = 0.44. \tag{20}$$

It is interesting to ask whether the measured squeezing after passing the squeezed field through the microscope is consistent with this measured total efficiency. The theoretical squeezed variance after transmission with an efficiency of η is $V_{\text{sqz}}^{\text{after}} = \eta V_{\text{sqz}} + 1 - \eta$, where V_{sqz} is the squeezed variance directly after the OPA crystal. V_{sqz} can be estimated from the measured squeezed variance prior to the microscope $V_{\text{sqz}}^{\text{prior}}$ using then relation $V_{\text{sqz}}^{\text{prior}} = \eta_{\text{det}} V_{\text{sqz}} + 1 - \eta_{\text{det}}$, with the efficiency $\eta_{\text{det}} = 0.65$ determined in Section 9.2. Under ideal operating conditions, $V_{\text{sqz}}^{\text{prior}} = 0.72$ (or -1.4 dB), as shown in Fig. S9. However, the operating conditions of the squeezed light source vary from experiment to experiment due to variations in the overlap between the OPA pump and the input Stokes field, and variation in the performance of the phase lock. This results in degraded performance in some experiments (for instance, see Fig. 3**a** in the main text, for which $V_{\text{sqz}}^{\text{prior}} = 1 - 0.22 = 0.78$). Overall, we find that from experiment to experiment $V_{\text{sqz}}^{\text{prior}}$ varies in the range $V_{\text{sqz}}^{\text{prior}} = 0.76 \pm 0.04$. From this, we find the range of variances for the amplitude squeezing directly after the OPA crystal of $V_{\text{sqz}} = 0.63 \pm 0.06$. After transmission through the microscope apparatus and photodetection with a combined efficiency of η, the predicted detected squeezing is $V_{\text{sqz}}^{\text{after}} = 0.84 \pm 0.03$. This is broadly consistent with our measurements after the microscope, with squeezed variance in Fig. 3**b** of the main text equal to 0.87, and that in the quantum image of polystyrene beads in Fig. 4**a** of the main text equal to 0.81. In the case of live cell imaging, significant efforts were made to improve the alignment of the system, including improvements in the overlap between pump and seed in the optical parametric oscillator generating squeezing, of the alignment of pump and Stokes in the Raman microscope, and of the microscope itself. Fresnel reflective losses were also lower at the water-glass interfaces between sample and coverslips, than at the air-glass interfaces when imaging dry polystyrene samples. This resulted in an improved squeezed variance of 0.74 (Fig. 4**b**).

11 Estimation of lower limit to concentration sensitivity

The lower limit to detectable concentration is reached where SNR=1. Since the SNR increases with averaging time, we use normalized units, equivalent to the sensitivity achievable for the

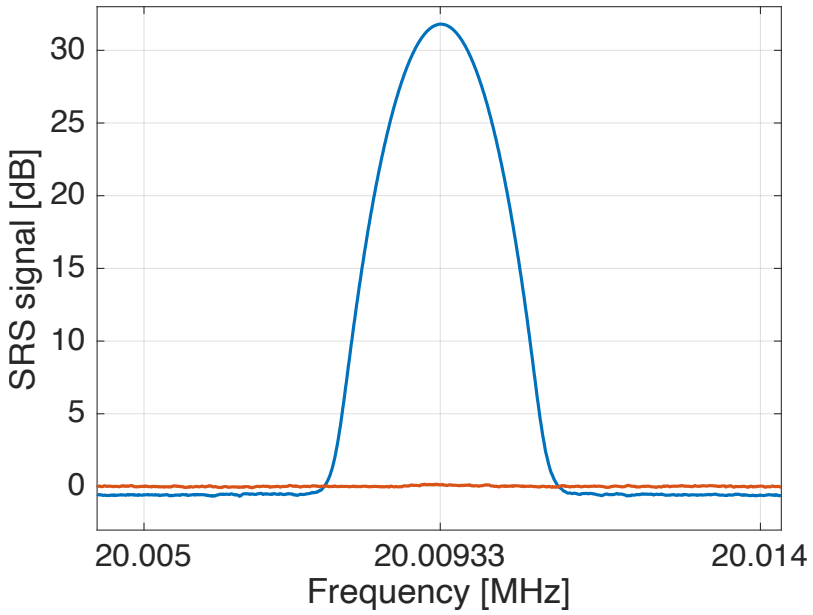

Figure S10: **Measurements used to determine concentration sensitivity.** Power spectral density of the detected photocurrent when probing the CH aromatic stretch band (Raman shift of 3055 cm^{-1}) in polystyrene. The spectral density shows the stimulated Raman signal and noise floor for the quantum-enhanced measurement (blue) together with the shot-noise-limited noise floor (red). The quantum-enhanced measurement has a signal-to-noise-ratio of 1730 and a noise floor suppressed by 13% (-0.58 dB) beneath the shot-noise limit. 30 mW of pump power and 3 mW of Stokes power were used. RBW: 1 kHz. VBW: 10 Hz.

case of 1 s acquisition time. It is possible to estimate this concentration by extrapolating how the measured SNR changes as the acquisition time changes and the concentration changes. The stimulated Raman signal amplitude scales linearly with concentration C. Since the SNR is linearly proportional to the power of the stimulated Raman signal, it therefore scales quadratically with concentration. Hence, the minimum detectable concentration is $C_{\mathrm{min}} = C/\mathrm{SNR}^{1/2}$. The SNR increases linearly with time so that the SNR in normalized units can be related to SNR(τ) for an arbitrary acquisition time τ via SNR(1 s)=SNR(τ)$\times$(1 s)/τ. We therefore find that the minimum detectable concentration can be found as $C_{\mathrm{min}} = C/\mathrm{SNR}(\tau)^{1/2} \times [\tau/(1\ \mathrm{s})]^{1/2}$.

Polystyrene is a polymer formed from the monomer styrene, and does not have a well-defined molecular weight or number of aromatic rings. However every aromatic ring corresponds to one styrene monomer. Using the density of polystyrene, 1060 kg/m^3, and the molecular weight of styrene, 104.15 g/mol, we therefore find the polystyrene concentration to be C = 10.2 M. Note that the unit M corresponds to mol/L.

Optimisation of the microscope for cell imaging also allowed significant improvements in the signal-to-noise of our polystyrene measurements. The highest damage-free shot-noise-limited signal-to-noise that we determine for the CH aromatic stretch bonds of polystyrene is 1510. This was recorded with 1 kHz resolution bandwidth which corresponds to an effective measurement time of $\tau = 1$ ms. Extrapolating to SNR=1 with 1 Hz resolution bandwidth, the minimum concentration sensitivity for styrene is estimated as $C_{\mathrm{min}} = 8.3$ mM $\mathrm{Hz}^{-1/2}$. The quantum enhanced SNR was

1730 (see Fig. S10), also recorded with 1 kHz resolution bandwidth. Similarly extrapolating this to SNR=1 provides an estimated minimum concentration sensitivity of $C_{\min} = 7.8$ mM $\mathrm{Hz}^{-1/2}$, enhanced by around 7% due to quantum correlations.

The sensitivity we achieve is broadly consistent with high performance stimulated Raman microscopes reported in the literature. Refs. [8] and [9] both perform stimulated Raman microscopy on the same CH aromatic stretch bond in polystyrene that we probe, allowing a quantitative comparison. A fair comparison requires that differences in pump and Stokes power are taken into account. In our experiments, the minimum detectable concentration scales linearly with pump power and as the square root of Stokes power, which were 30 mW and 3 mW respectively. As such our minimum resolvable concentration can be normalized to $C_{\min} = 400$ mM $\mathrm{Hz}^{-1/2}$ $\mathrm{mW}^{-3/2}$.

Ref. [8] reports a shot-noise-limited stimulated Raman microscope using a two-color scheme to improve signal-to-noise by subtracting common mode noise on a balanced detector. A maximum signal-to-noise of 106 is reported, using 28 mW of Stokes power, 14 mW of pump power and a total integration time of 0.1 ms. They detect the pump, rather than the Stokes, so that the power dependences of the signal-to-noise are reversed compared to our experiments. Two alternative definitions of signal-to-noise are common in the literature, the ratio of signal power to noise power used in our work, and the ratio of signal amplitude to noise standard deviation. Ref. [8] does not specify which definition they use. Assuming the same definition as we use, we infer from the numbers above a minimum resolvable concentration of around 1040 mM $\mathrm{Hz}^{-1/2}$ $\mathrm{mW}^{-3/2}$. With the alternative definition, the minimum resolvable concentration is around 101 mM $\mathrm{Hz}^{-1/2}$ $\mathrm{mW}^{-3/2}$. Either way, the sensitivity is similar to our best reported sensitivity, with one definition of signal-to-noise yielding a factor of 2.6 higher sensitivity, and the other a factor of 4 lower.

Ref. [9] makes measurements using both simultaneous Raman gain and stimulated Raman loss detection modes, using a 0.25 ms integration time. Of these, the most direct comparison to our experiments comes from the simultaneous Raman gain measurements, since this is the detection mode we use. For these measurements, they use 10 mW of power for both pump and Stokes. They record an amplitude signal-to-noise of 23.1 which corresponds to a power signal-to-noise of $23.1^2 = 534$. Using these numbers we infer a concentration sensitivity of 220 mM $\mathrm{Hz}^{-1/2}$ $\mathrm{mW}^{-3/2}$, around a factor of 1.8 lower than our best reported sensitivity. For their stimulated Raman loss measurements, they use 8 mW of Stokes power and 6 mW of pump power, and report an amplitude signal-to-noise of 27.0 (power signal-to-noise of $27.0^2 = 730$). From these numbers we infer an improved concentration sensitivity of 140 mM $\mathrm{Hz}^{-1/2}$ $\mathrm{mW}^{-3/2}$. This is a factor of 2.9 lower than our experiments, though not directly comparable since the measurement uses stimulated Raman loss rather than gain.

The above comparisons show that the concentration sensitivity from our experiments is similar to those reported for the same bond in polystyrene in other stimulated Raman microscopes. Apart from the modest 7% improvement provided by quantum correlations in our case, the variations between experiments most likely arise primarily from the difference in pulse durations – both Refs. [8] and [9] use few-hundred femtosecond pulses compared to our picosecond pulses. Differences in collection efficiency and optical focussing into the microscope can also be expected to contribute to the variation, though to a lesser degree.

We would note that the concentration sensitivity that can be achieved depends strongly on the particular molecular vibration that is probed. For example, a state-of-the-art stimulated Ra-

man microscope was reported to allow measurement of CH bonds in dimethyl sulfoxide (DMSO) with a concentration limit of 28 mM with 2 μs time constant, and with pump and Stokes powers of 72 mW and 20 mW [10, 11]. This corresponds to a minimum concentration sensitivity of 12.8 mM $\mathrm{Hz}^{-1/2}$ $\mathrm{mW}^{-3/2}$, a factor of approximately thirty times lower than our system. Other bonds with especially high Raman cross-sections allow even better concentration sensitivity. For instance, sensitivities in the tens of micromolar range have be achieved for the alkyne bond (C≡C) [11, 12, 13, 14].

12 Imaging

The quantum-enhanced images are formed by recording the stimulated Raman signal on the spectrum analyser while raster scanning the sample in 100 nm steps at a rate of 20 steps per second, returning a 100×100 pixel image in 8.3 minutes. The stage position is recorded throughout the raster scan and is used to assign positions to the measured Raman values. After recording the stimulated Raman signal at each position, the shot-noise is also measured at each of the same locations by blocking the pump field, keeping the Stokes power at the detector at 3 mW, and recording shot-noise across a similar raster scan. The Raman signal is normalized by dividing by the shot-noise level at the same locations, which corrects for any change in signal strength due to attenuation of the detected Stokes field by the sample.

12.1 Yeast cell images

As described in the main text, our images of yeast cells show three key features, a relatively uniform signal across the entire cell that likely originates from cytosol, five bright roughly-ellipsoidal shapes, and a faint sub-200 nanometre-thick semicircular feature. The Raman shift of 3055 cm^{-1} used to generate the images was chosen to selectively target lipids. The five roughly-ellipsoidal shapes seen in Fig. 4**b** of the main text are likely to be lipid droplets, since multiple lipid droplets of this shape and size are commonly observed in yeast cells (see e.g. Refs. [15, 16, 17]). The semicircular feature is consistent in shape with a section of the cell membrane or wall. While the cell membrane consists of lipids and the cell wall has a significant fraction of lipid [18], their tens-of-nanometre thickness results in far weaker Raman signals than large structures such as lipid droplets, consistent with what we observe. The weakness of the Raman signal could explain why we only observe a semicircular feature rather than a full circle enclosing the cell contents, with the Raman signal sinking beneath the optical noise (even though it is reduced using quantum correlations) across the majority of the structure. Measurements that only partially resolve the cell membrane are not uncommon in Raman imaging. For examples, see Ref. [19] where the Raman signal varies strongly at different parts of the membrane, and Ref. [20] where it is only partially resolved. It is also conceivable that this feature arises from some form of aberration, distortion, scattering or transmission effect.

The straight horizontal line of high Raman signal visible in Fig. 4**b** is an artefact that we attribute to optical trapping of a high-Raman-contrast particulate by the Raman pump laser. The particulate was then held stationary for some time within the optical excitation area as the sample stage

and cell were scanned, before becoming untrapped prior to a single line scan being completed. Our scanning system was arranged to scan horizontally and then step vertically, consistent with this hypothesis.

We determine the peak Raman signal at the lipid-droplet-like features to be 23 dB relative to the quantum-enhanced noise floor. From this, the maximum signal-to-noise of the Raman signal arising from these features may be calculated as SNR= $10^{(23-3)/10} = 100$, where the subtraction of 3 dB is present since a Raman signal relative to the quantum-enhanced noise floor of 3 dB has equal contributions from the quantum noise and genuine Raman signals from the specimen, and therefore corresponds to a signal-to-noise of one. Similarly, we average the Raman signal in an interior region of the cell free of lipid particles to obtain the cytosol Raman signal of 7.7 dB relative to the quantum-enhanced noise floor, and signal-to-noise ratio of 3. Since quantum light increases the signal-to-noise ratio by 35%, the shot-noise limited signal-to-noise ratios can be obtained from the quantum-enhanced ones by dividing by the 1.35.

It is interesting to compare the cell images generated by our quantum-enhanced microscope (shown in Fig. 4**b** of the main text) to previously reported yeast cell images using Raman microscopy. Here, we compare to images previously reported using both coherent Raman microscopy [21, 16, 22] and spontaneous Raman microscopy [15]. The shortest reported pixel dwell time in these experiments is 50 ms [21], the same as was used in our experiments. In this case fourteen Raman lines were probed simultaneously, in contrast to our single line, and the peak signal-to-noise was around 5, compared to our peak signal-to-noise of 100. Ref. [16] does not report a pixel dwell time, but also has a signal-to-noise of around 5. The other two experiments have pixel dwell times in the range of 0.1-0.5 seconds, significantly longer than ours. We were unable to extract the signal-to-noise in these cases.

12.2 Observation of yeast cell photodamage

In addition to quantifying the optical damage on polystyrene beads, we were able to observe and illustrate light-induced damage on the yeast cells. Photodamage appeared for intensities of 470 W/μm^2. We document in Figure S11**g** a case of photodamage occurring during a scan. The image was scanned in horizontal scans, stepping vertically between scans and starting an the bottom of the image. The signal amplitude increased considerably after the appearance of visible damage. The Raman signal increased by up to 40 dB and debris with high Raman signatures were dragged outside of the cell by the horizontal motion of the beam. We also present in Figure S11 widefield images of damaged cells. The damage was often localized and associated with shrinking. This suggests that the light may have caused membrane destruction followed by diffusion of the organelles into the extracellular medium.

12.3 Comparison of squeezed and shot noise limited images

Figure S12 compares a quantum enhanced cell image (Fig. S12**a**), to the equivalent shot-noise limited image obtained by artificially raising the noise floor to the shot noise floor (Fig. S12**b**), and to an experimental shot noise limited image (Fig. S12**c**). The removal of quantum correlated light

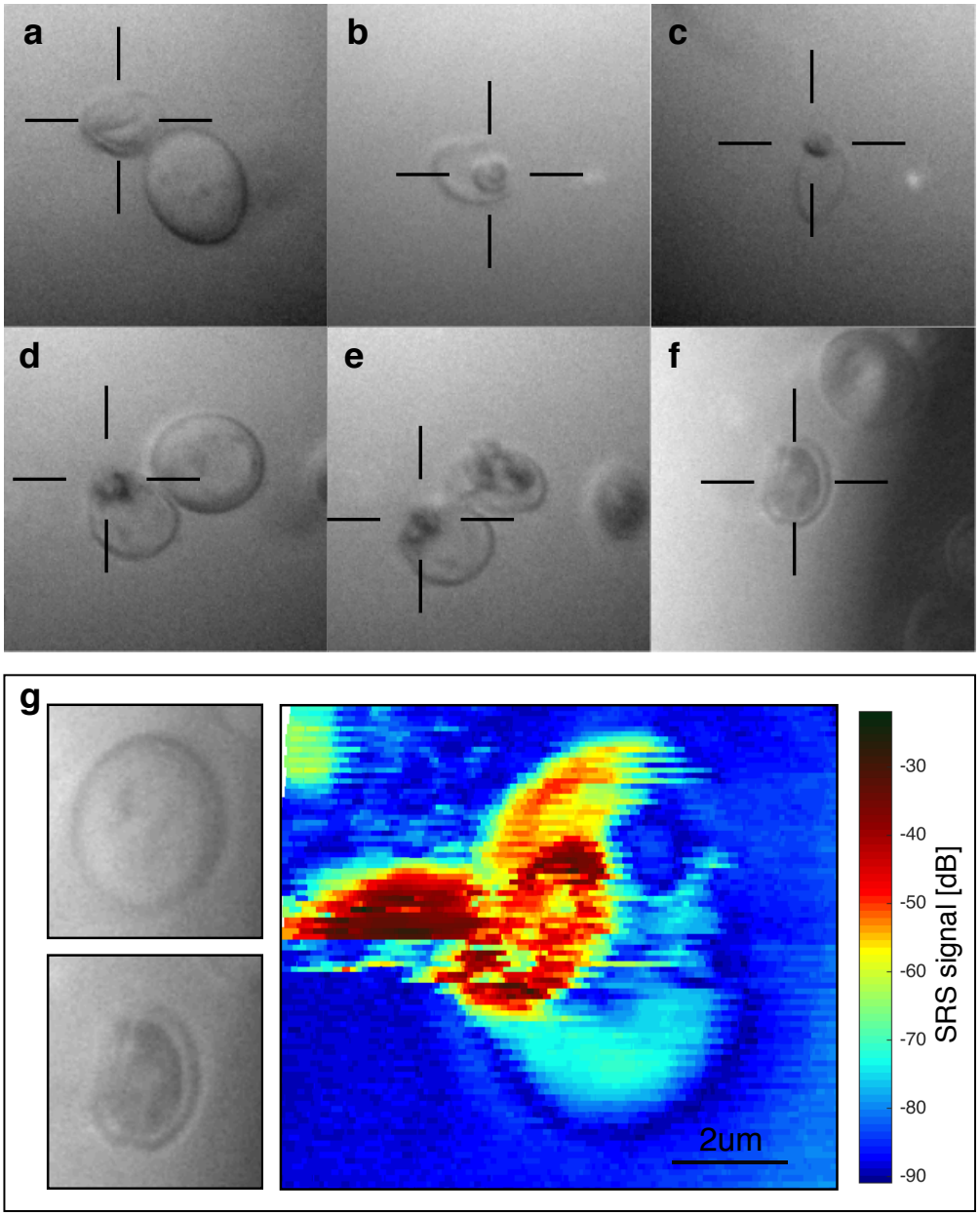

Figure S11: **Bright-field images and Raman signal image of damaged yeast cells.** Photodamage induced by the pump field on yeast cells with 30 mW of pump power at the sample and an effective microscope objective numerical aperture of $NA_{effective} \sim 1.2$, corresponding to an intensity of around 470 W/μm^2. **a** to **f**: widefield images of damaged cells. **g**: Photodamage induced during simulated Raman imaging. Left: widefield images before (top) and after (bottom) damage. Right: Raman image showing damage occurring mid-scan.

in Fig. S12**b**&**c** results in an evident reduction in contrast. The experimental shot noise limited image was taken 30 minutes after the quantum-enhanced image. The sample was found to drift axially over these timescales. We attribute the degradation in resolution observable in Fig. S12**c** to this drift, rather than the removal of quantum correlations. Fig. S12**d** plots the Raman signal along the dashed cross sections on Figs. S12**a**&**b**, where the semi-circular feature that may be the membrane is well resolved both for the quantum enhanced and shot-noise limited equivalent images. Fig. S12**e** is the same plot in a region of the membrane-like feature where only the quantum enhanced image resolves the feature with a signal-to-noise ratio higher than 1.

One way to illustrate the advantage provided by quantum correlations is to analyse the images for features that are not resolvable without these correlations. As can be seen by comparing the images in Figure S12**a**,**b** & **c**, the semicircular feature located vertically above main body of cell (consistent with a segment of the cell membrane or wall) is significantly better resolved using quantum correlations than without them. To quantify this improvement we estimate the resolvable fraction of this feature for Figures S12 **a** and **b**[3]. This is done by taking radial cross-sections of the images through the feature, and interpolating the Raman signal along these cross-sections. The cross-sections show a small bump at the feature (see Fig. S12**d** &**e**), which we define as resolvable if its maximum is more than a factor of two higher than the noise floor (equalling a signal-to-noise of 1). This yields an angular range for which the signal from the feature is resolvable for each of the quantum-enhanced and shot-noise limited images. From this analysis, we found that the quantum-enhanced image allows a 40% greater length of the feature to be resolved than the shot-noise limited image. Assuming the feature to be roughly circular as expected for the cell membrane or wall, this corresponds to 23% of the total feature, compared to 16% for the shot-noise limited image (shown angularly by the double-headed angles in Figs. S12**a** & **b**).

13 Other approaches to evade photodamage

It is interesting to ask what avenues might be available, other than quantum correlations, to evade photodamage in biological imaging. An obvious approach is to introduce contrast enhancing labels such as in Ref. [23]. However, this comes at the risk of the contrast label compromising the natural behaviour of the specimen. An alternative would be to increase the pixel dwell time, allowing longer acquisitions and therefore higher signal-to-noise for a fixed illumination intensity. In this case, the signal-to-noise scales linearly with pixel dwell time (assuming that the pulse duration, peak intensity and repetition rate are fixed), so that a 35% enhancement in signal-to-noise, such as is demonstrated here, could be obtained using a 35% longer measurement. This assumes, however, that the photodamage is due to the intensity of the illumination light. This is not always the case. For instance, the buildup of reactive oxygen species due to optical illumination is one key cause of photodamage. This build-up typically depends on the total irradiation energy rather than the intensity, and so cannot be avoided by performing a longer but lower-intensity measurement.

In non-linear microscope such as coherent Raman microscopes, imaging frame-rate is a crucial concern due to the weakness of the non-linear scattering cross sections [11]. In Raman microscopy

[3]We do not attempt to quantitatively compare the quantum enhanced image to Figure S12**c** both because of the degradation in resolution in that image; and because switching the squeezed light source on changes the spatiotemporal profile of the Stokes beam making a quantitative comparison invalid (see Section 8.3).

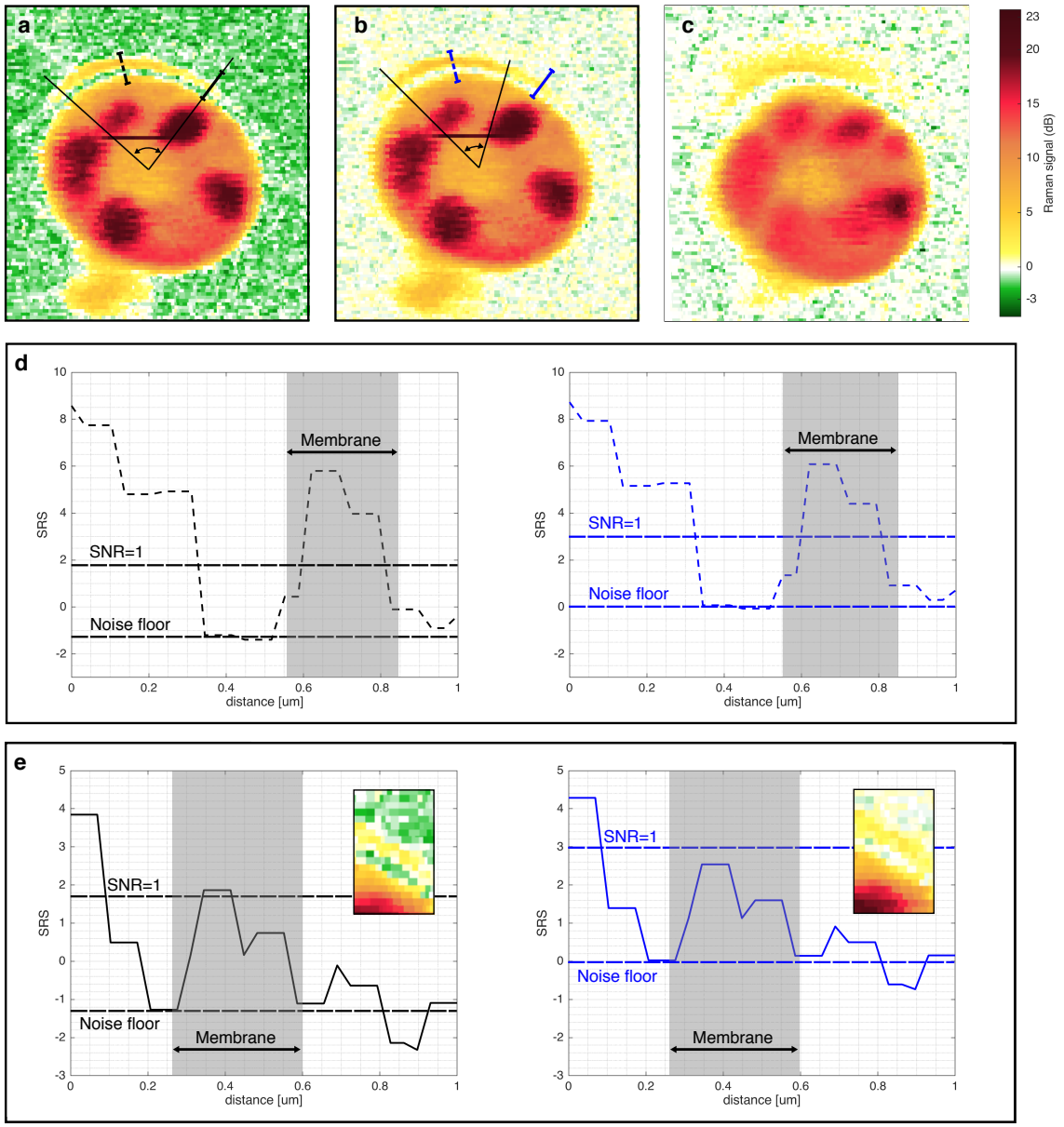

Figure S12: **Comparison of quantum-enhanced and shot-noise limited images.** **a**,**b** & **c** respectively show the quantum-enhanced image, shot-noise limited image produced by artificially raising the background of the quantum enhanced image by 1.3 dB, and the shot-noise limited image. An interpolation of the Raman signal is performed radially from the center of the cell to quantify the resolvable fraction of the membrane-like feature. **d** Raman signals along the dashed lines in **a** & **b**, corresponding to the cross-section with maximum signal-to-noise from the feature. Here we see SRS signals are approximately 7 and 6 dB higher than the noise floor, respectively, for the quantum-enhanced and shot-noise limited images. **e** Raman signals along the solid lines in **a** & **b**, corresponding to cross-section with degraded feature signal-to-noise. Here the SRS signals are approximately 3.1 and 2.5 dB higher than the noise floors, respectively, for the quantum-enhanced and shot-noise limited images. In this case, only the quantum-enhanced measurements has a signal-to-noise above one. In **d**&**e**: insets are magnified parts of the Raman images, showing the membrane-like feature; grey shading shows the location of the membrane-like feature; upper dashed horizontal lines show a signal-to-noise of one; and lower dashed horizontal lines show the noise floor normalised to the shot-noise level.

this is especially true, since it is in principle possible to perform parallel multispectral imaging [23] to extract very reach chemical information about the specimens under study, but this requires multiple measurements at different Raman shifts and often requires probing of molecular bonds with far weaker Raman cross sections than C-H bonds. As such, compromises that involve increased measurement duration are not typically preferable.

The absolute quantum advantage we report is defined relative to classical experiments conducted with the same spatiotemporal modeshapes and apparatus. It is also interesting to consider what avenues might be available to improve signal-to-noise without quantum correlations, were these conditions to be relaxed.

An obvious path to improvements, both for shot-noise limited and quantum-enhanced Raman microscopy would be to improve the efficiency of the microscope, as well as of the optical components after it (and in the case of quantum-light, also between the squeezed light source and the microscope). In our case, the total efficiency for squeezed light was around 40%, and somewhat higher for the transmission fo the probe light through the microscope. As such, improvements in signal-to-noise from enhanced efficiency are possible, but constrained (without quantum-correlations, changing the pulse focussing/width, or increasing the light intensity at the sample) to a maximum of around a factor of two. Improvements using quantum-correlation do not suffer this constraint, in principle allowing arbitrarily high signal-to-noise. For example, a factor of thirty enhancement has been demonstrated using continuous wave technology developed for gravitational wave detection [24].

The signal-to-noise could also potentially be improved through careful tuning of the pulse widths of the pump and Stokes fields. As discussed already in the main text and in Section 2 of the Supplementary Information, these widths should be roughly matched to the decay time of the Raman transition that is being probed. In biology, these widths tend to be in the picosecond range, matching the pulse widths we have chosen for SRS system. Indeed, we based our system design on previous literature on precision stimulated Raman microscopes (see e.g. Ref. [25]), taking care to choose appropriate pulse width and repetition rate to give a strong Raman signal, while also aiming to minimise photodamage (i.e. ultimately to maximise the signal-to-noise ratio). We believe that the signal-to-noise of our system is close to optimised, in this respect. Nevertheless, the exact optimal pulse width and repetition rate will vary from specimen to specimen and between Raman transitions within a given specimen.

References

[1] Yan Fu, Haifeng Wang, Riyi Shi, and Ji-Xin Cheng. Characterization of photodamage in coherent anti-stokes Raman scattering microscopy. *Optics Express*, 14(9):3942–3951, 2006.

[2] Michael A Taylor and Warwick P Bowen. Quantum metrology and its application in biology. *Physics Reports*, 615:1–59, 2016.

[3] Christian W Freudiger, Wei Min, Brian G Saar, Sijia Lu, Gary R Holtom, Chengwei He, Jason C Tsai, Jing X Kang, and X Sunney Xie. Label-free biomedical imaging with high sensitivity by stimulated Raman scattering microscopy. *Science*, 322(5909):1857–1861, 2008.

[4] Brian G Saar, Christian W Freudiger, Jay Reichman, C Michael Stanley, Gary R Holtom, and X Sunney Xie. Video-rate molecular imaging *in vivo* with stimulated Raman scattering. *Science*, 330(6009):1368–1370, 2010.

[5] Alexander A Oraevsky, Luiz B Da Silva, Alexander M Rubenchik, Michael D Feit, ME Glinsky, Michael D Perry, Beth M Mammini, W Small, and Brent C Stuart. Plasma mediated ablation of biological tissues with nanosecond-to-femtosecond laser pulses: relative role of linear and nonlinear absorption. *IEEE Journal of Selected Topics in Quantum Electronics*, 2(4):801–809, 1996.

[6] Takahiro Serikawa and Akira Furusawa. 500 mhz resonant photodetector for high-quantum-efficiency, low-noise homodyne measurement. *Review of Scientific Instruments*, 89(6):063120, 2018.

[7] Gil Triginer Garces, Helen M Chrzanowski, Shakib Daryanoosh, Valerian Thiel, Anna L Marchant, Raj B Patel, Peter C Humphreys, Animesh Datta, and Ian A Walmsley. Quantum-enhanced stimulated emission detection for label-free microscopy. *Applied Physics Letters*, 117(2):024002, 2020.

[8] Youngjin Choi, Sohee Lim, Joong Won Shim, Bonghwan Chon, Jong Min Lim, and Minhaeng Cho. Shot-noise-limited two-color stimulated Raman scattering microscopy with a balanced detection scheme. *The Journal of Physical Chemistry B*, 124(13):2591–2599, 2020.

[9] Rajeev Ranjan, Annalisa Darco, Maria Antonietta Ferrara, Maurizio Indolfi, Michele Larobina, and Luigi Sirleto. Integration of stimulated Raman gain and stimulated Raman losses detection modes in a single nonlinear microscope. *Optics Express*, 26(20):26317–26326, 2018.

[10] Ke Wang, Delong Zhang, Kriti Charan, Mikhail N Slipchenko, Ping Wang, Chris Xu, and Ji-Xin Cheng. Time-lens based hyperspectral stimulated Raman scattering imaging and quantitative spectral analysis. *Journal of Biophotonics*, 6(10):815–820, 2013.

[11] Ji-Xin Cheng and X Sunney Xie. Vibrational spectroscopic imaging of living systems: An emerging platform for biology and medicine. *Science*, 350(6264):aaa8870, 2015.

[12] Lu Wei, Fanghao Hu, Yihui Shen, Zhixing Chen, Yong Yu, Chih-Chun Lin, Meng C Wang, and Wei Min. Live-cell imaging of alkyne-tagged small biomolecules by stimulated Raman scattering. *Nature Methods*, 11(4):410–412, 2014.

[13] Senlian Hong, Tao Chen, Yuntao Zhu, Ang Li, Yanyi Huang, and Xing Chen. Live-cell stimulated Raman scattering imaging of alkyne-tagged biomolecules. *Angewandte Chemie*, 126(23):5937–5941, 2014.

[14] Hyeon Jeong Lee, Wandi Zhang, Delong Zhang, Yang Yang, Bin Liu, Eric L Barker, Kimberly K Buhman, Lyudmila V Slipchenko, Mingji Dai, and Ji-Xin Cheng. Assessing cholesterol storage in live cells and C. elegans by stimulated Raman scattering imaging of phenyl-diyne cholesterol. *Scientific Reports*, 5(1):1–10, 2015.

[15] Kamila Kochan, Huadong Peng, Bayden R Wood, and Victoria S Haritos. Single cell assessment of yeast metabolic engineering for enhanced lipid production using Raman and AFM-IR imaging. *Biotechnology for Biofuels*, 11(1):106, 2018.

[16] Fredrik Svedberg, Christian Brackmann, Thomas Hellerer, and Annika M Enejder. Nonlinear microscopy with fiber laser continuum excitation. *Journal of biomedical optics*, 15(2):026026, 2010.

[17] www.leica-microsystems.com/science-lab/obese-and-slim-yeast-cells. Accessed: 2020-09-27.

[18] JB Rattray, Angelo Schibeci, and Denis K Kidby. Lipids of yeasts. *Bacteriological Reviews*, 39(3):197, 1975.

[19] Matthias Hofer, Naveen K Balla, and Sophie Brasselet. High-speed polarization-resolved coherent Raman scattering imaging. *Optica*, 4(7):795–801, 2017.

[20] Gianluigi Zito, Giulia Rusciano, Giuseppe Pesce, Alden Dochshanov, and Antonio Sasso. Surface-enhanced Raman imaging of cell membrane by a highly homogeneous and isotropic silver nanostructure. *Nanoscale*, 7(18):8593–8606, 2015.

[21] Masanari Okuno, Hideaki Kano, Philippe Leproux, Vincent Couderc, James PR Day, Mischa Bonn, and Hiro-o Hamaguchi. Quantitative CARS molecular fingerprinting of single living cells with the use of the maximum entropy method. *Angewandte Chemie*, 122(38):6925–6929, 2010.

[22] Ryo Furuta, Naoyuki Kurake, Kenji Ishikawa, Keigo Takeda, Hiroshi Hashizume, Hiroki Kondo, Takayuki Ohta, Masafumi Ito, Makoto Sekine, and Masaru Hori. Intracellular-molecular changes in plasma-irradiated budding yeast cells studied using multiplex coherent anti-stokes Raman scattering microscopy. *Physical Chemistry Chemical Physics*, 19(21):13438–13442, 2017.

[23] Lu Wei, Zhixing Chen, Lixue Shi, Rong Long, Andrew V Anzalone, Luyuan Zhang, Fanghao Hu, Rafael Yuste, Virginia W Cornish, and Wei Min. Super-multiplex vibrational imaging. *Nature*, 544(7651):465–470, 2017.

[24] Henning Vahlbruch, Moritz Mehmet, Karsten Danzmann, and Roman Schnabel. Detection of 15 db squeezed states of light and their application for the absolute calibration of photoelectric quantum efficiency. *Physical Review Letters*, 117(11):110801, 2016.

[25] Christian W Freudiger, Wenlong Yang, Gary R Holtom, Nasser Peyghambarian, X Sunney Xie, and Khanh Q Kieu. Stimulated Raman scattering microscopy with a robust fibre laser source. *Nature Photonics*, 8(2):153, 2014.